COMPUTERS AND ELECTRONICS IN AGRICULTURE 60 (2008) 67–75

available at www.sciencedirect.com

ScienceDirect

journal homepage: www.elsevier.com/locate/compag

Creating a panoramic field image using multi-spectral stereovision system

M. Kise[a,1], Q. Zhang[b,*]

[a] United States Department of Agriculture, Agricultural Research Service Russell Research Center, 950 College Station Road, Athens, GA 30605, USA

[b] Department of Agricultural and Biological Engineering, University of Illinois at Urbana-Champaign, 1304 W. Pennsylvania Ave., Urbana, IL 61801, USA

ARTICLE INFO

Article history:
Received 24 February 2006
Received in revised form
15 June 2007
Accepted 2 July 2007

Keywords:
Image mosaic
Multi-spectral field images
3D panoramic field images
Stereovision
Ground-based remote sensing

ABSTRACT

Satellite-based remote sensing presents a broad view of field scenes while ground-based remote sensing offers detailed observation of the crop to support precision farming decision-making. If it is possible to combine the advantages of both satellite-based and ground-based sensing, the resulting imagery could present both the broad view of a field scene and detailed observation of crop growth, which offers a very informative means for delivering crop production information. This paper describes a fundamental investigation on creating multi-spectral 3D panoramic field imagery by seamlessly integrating ground-based multi-spectral images of the field. A vehicle-mounted stereovision sensor composed of two multi-spectral cameras collects six-spectral channel images to form the multi-spectral 3D field imagery. The collected stereo image stream is then synthesized progressively to create a single seamless field image. The resulting panoramic imagery forms a 3D virtual field scene capable of providing more informative interpretation of crop/field status than a 2D plane image. Field test results proved that the assembled multi-spectral imagery was capable of providing a seamless 3D panoramic view of a soybean field with a broad view for assessing crop growth status with sufficient detail of individual crop plants.

© 2007 Elsevier B.V. All rights reserved.

1. Introduction

Image-based remote sensing can remotely sense the property of crops in the field by means of measuring spectral reflectance from crop canopies. A remote sensing system can acquire satellite, airborne or ground-based images relative to the type of platform carrying the imaging sensor. The major difference of the three platforms is their viewpoint height, which dominates the spatial resolution and image field of view. Among the three types of images, satellite imagery has the highest viewpoint. Hence, it covers the largest field of view, but with the lowest spatial resolution in general. Naturally, satellite-based remote sensing is often used for the applications requiring wide area coverage but not high spatial resolution, such as the classification of crop types (Maxwell et al., 2004; Van Niel and McVicar, 2004) and the estimation of spatial distribution of water content in the soil (Cashion et al., 2004). In contrast with satellite imagery, ground-based imagery offers high spatial resolution to make individual leaves on a plant distinguishable, and therefore is suited for applications requiring a plant-level spatial resolution. Examples of such applications are plant population counting and

* Corresponding author. Tel.: +1 217 333 9419; fax: +1 217 244 0323.
E-mail address: qinzhang@uiuc.edu (Q. Zhang).
[1] Tel.: +1 706 546 3454; fax: +1 706 546 3633.

0168-1699/$ – see front matter © 2007 Elsevier B.V. All rights reserved.
doi:10.1016/j.compag.2007.07.002

weed mapping (Tillett et al., 2001; Shrestha and Steward, 2003). Furthermore, because ground-based vegetation indices are not affected by the atmosphere, special indices can be used that make use of information in wavelengths not restricted to atmospheric windows (Datt, 1999). The major drawback for ground-based sensing is its small field of view that requires acquiring a sequence of images in order to cover the large area. While airborne-based remote sensing can provide a compromise between satellite-based and ground-based imagery in terms of spatial resolution and field coverage, professional service providers are required to fly the aircraft for capturing field images, which often brings additional costs, as well as the scheduling difficulties to producers.

Ideally, a remote sensing image should have a wide view to cover the entire field and have a high resolution to present the growth information of an individual crop plant. Enhancing image resolution and widening field of view simultaneously is a trade-off problem for conventional remote sensing. However, if it would be possible to obtain a stream of high resolution images, such as a video sequence acquired from a ground-based moving platform, and then subsequently merging those images into one seamless image, a field image of unlimited coverage with a high resolution would be obtained. In this research, a ground-based remote sensing platform that acquires a stream of multi-spectral 3D field images using a vehicle-mounted stereo camera was developed. The objective of this research was to develop a remote sensing system that could provide information of the entire field with great detail. More specifically, a field image of:

(1) a seamless panoramic view with high spatial resolution,
(2) three-dimensional (3D) information of plants,
(3) spectral reflectance in multiple bands.

was to be created by synthesizing ground-based images.

Regarding (1), image processing that stitches a stream of images into an integrated panoramic image is called image mosaicing. There have been several agricultural remote sensing systems that mosaic multiple images together and create a panoramic image reported previously, but most of them are based on either aerial or satellite images with spatial resolution up to a meter or greater, depending on altitude (Wright et al., 2003; Thomson et al., 2005). In contrast, a typical ground-based imagery obtains spatial resolution on the order of millimeters and requires more precision alignment to create a seamless mosaic image as compared with the precision required for aerial or satellite image mosaicing. However, it is worthy to be pointed out comparing to the capability of acquiring a regional farmland remote sensing imagery by one shot, the proposed method needs to take numerous shots then integrate the individual images to form an complete imagery for the field of interest, and this process is often time consuming.

The image sensor installed on the ground-based platform is a stereovision camera composed of two multi-spectral cameras. A stereo camera consists of two identical cameras with their optical axis being geometrically arranged in parallel. A stereo image attains the 3D field scene information by means of taking the same field scene from slightly offset viewpoints using two cameras. The additional dimension of the scene often provides some critical information for many applications. Recently, successful applications of using a stereovision system in agriculture have been reported, such as stereovision-based tractor guidance (Kise et al., 2005), crop and animal growth condition observation, and physical parameter estimation (Lines et al., 2001; He et al., 2003; Rovira-Más et al., 2005), and livestock 3D shape extraction (Wu et al., 2004). By taking advantage of stereovision, the imaging system developed in this research can provide useful 3D plant information, such as the height and volume of plants along with the spectral reflectance, which satisfies second the condition of the above list. A single lens camera or spectral sensor has been traditionally used to obtain crop biophysical information; however, they can only estimate such biophysical parameters from the sensor outputs (Goel et al., 2003; Payero et al., 2004). Consequently, the outcomes obtained from those traditional sensors are dependent upon many factors, such as the variety of the plant, local climate and field management.

Finally, each camera consists of three charge coupled device (CCD) sensors with different spectral filters, which allows the system to capture field images in three spectral bands. Because two cameras have different spectral configurations, a composite image of two cameras contains six-spectral channels. The spectral reflectance from the plants can indicate plant growth status. Numerous indices have been developed from various combinations of different bands of reflectance for estimating vegetation and soil parameters, such as nitrogen stress (Han et al., 2002), weed density (Bajwa and Tian, 2001), and soil nutrient composition and texture (Thomasson et al., 2001). This technology has also been used in yield prediction (Yang et al., 2001).

The following sections introduce the experimental system used in this research and development of a method for forming panoramic imagery. The developed remote sensing system was tested in the field to evaluate the precision of panoramic field image creation.

2. Experimental systems

2.1. *Multi-spectral stereo camera and test platform*

The stereovision camera was composed of two multi-spectral CCD cameras (MS-3100, Redlake Inc., San Diego, CA). Both cameras have three high-resolution CCD imagers capable of acquiring field images in three spectral bands, as shown in Table 1. This configuration allows the stereovision camera to capture field images in six-spectral bands from visible to near infrared. Two cameras were aligned in parallel on the frame with a 102 mm separation on their optical axes to form a stereo camera. Both cameras were equipped with a 14 mm lens (Sigma, Kawasaki, Japan). An external trigger signal was used to control both cameras for synchronizing the image acquisition timing. The pair of images were acquired using two CameraLink frame grabbers (IMAQ PCI-1428, National Instruments, Austin, TX) at 5 frames/s. Stereo computation was performed on channel 2 of the left camera (CWL 537 nm)

Table 1 – Spectrum configuration of the stereo camera

Channel number	Left camera (MS3100 RGB)		Right camera (MS3100 CIR)	
	Center wavelength (nm)	FWHM (nm)	Center wavelength (nm)	FWHM (nm)
1	478	50	547.5	40
2	537	50	667.5	40
3	621	60	796	60

Fig. 1 – Research platform.

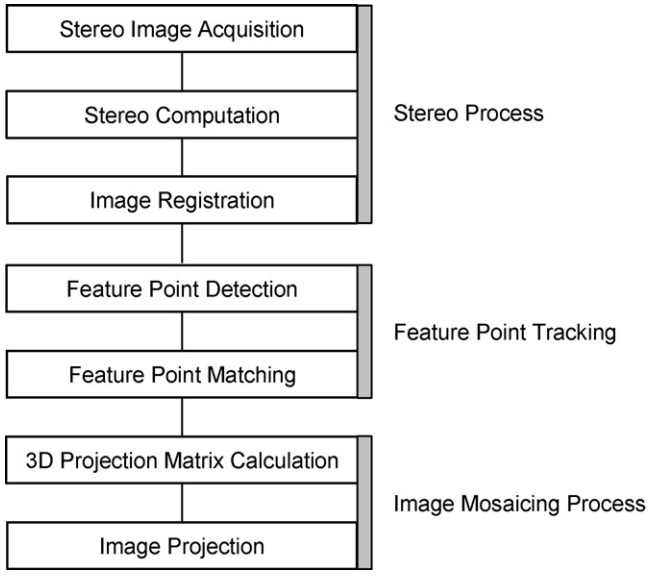

Fig. 2 – Conceptual flowchart of panoramic image formation algorithm.

and channel 1 of the right camera (547.5 nm) since they were the closest combination of wavelengths among all combinations.

Fig. 1 shows that the multi-spectral stereo camera was installed on a mobile research platform based on a high clearance agricultural sprayer. The stereo camera was mounted on a camera frame in front of the platform 3.8 m above ground level and viewed downward with very small forward tilt angle. This installation resulted in a field of view of 1.5 m × 0.8 m about 1.0 m in front of the platform. An RTK-GPS receiver (MS750, Trimble, Sunnyvale, CA), the measurement accuracy of which was ±2 cm, was also installed directly over the camera to record the vehicle trajectory.

2.2. *3D panoramic field image creation algorithm*

Creation of a panoramic field image is performed progressively by stitching consequent images of a vehicle-mounted multi-spectral stereo camera. Fig. 2 shows the basic procedures of 3D panoramic field image creation. The first step was stereo processing that extracts three-dimensional (3D) information of the field scene and registers two images of the multi-spectral cameras for creating a six-spectral band image. It was followed by the feature point tracking, which involves detecting points that had distinctive features and then finding their correspondences in adjacent images. Constituent images were then projected on the panoramic field image coordinates progressively based on the geometric relationship of the adjacent images calculated from the correspondence of feature points. All algorithms were developed in Microsoft Visual C++ environment.

2.3. *Stereo computation*

As the stereo geometry illustrates in Fig. 3, a stereovision camera is a vision sensor consisting of two identical cameras geometrically arranged parallel to each other. Assume both image planes are laid on the same plane with their horizontal axes being aligned; if a given global point (x_c, y_c, z_c) is projected at (x_i^L, y_i^L) in Image L and at (x_i^R, y_i^R) in image R (x_c, y_c, z_c) in

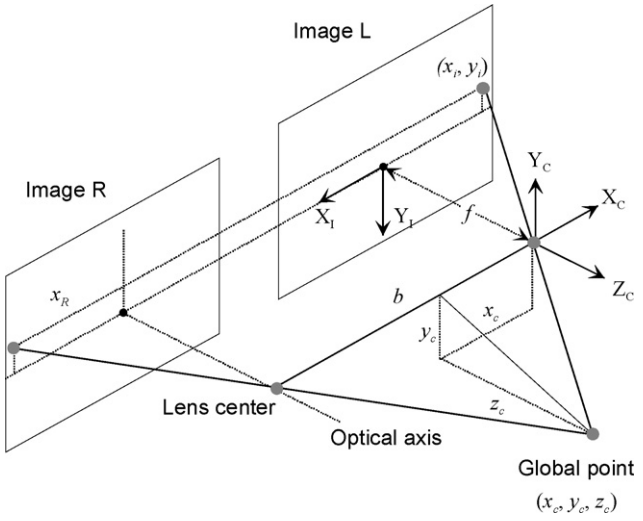

Fig. 3 – Principle of stereovision geometry.

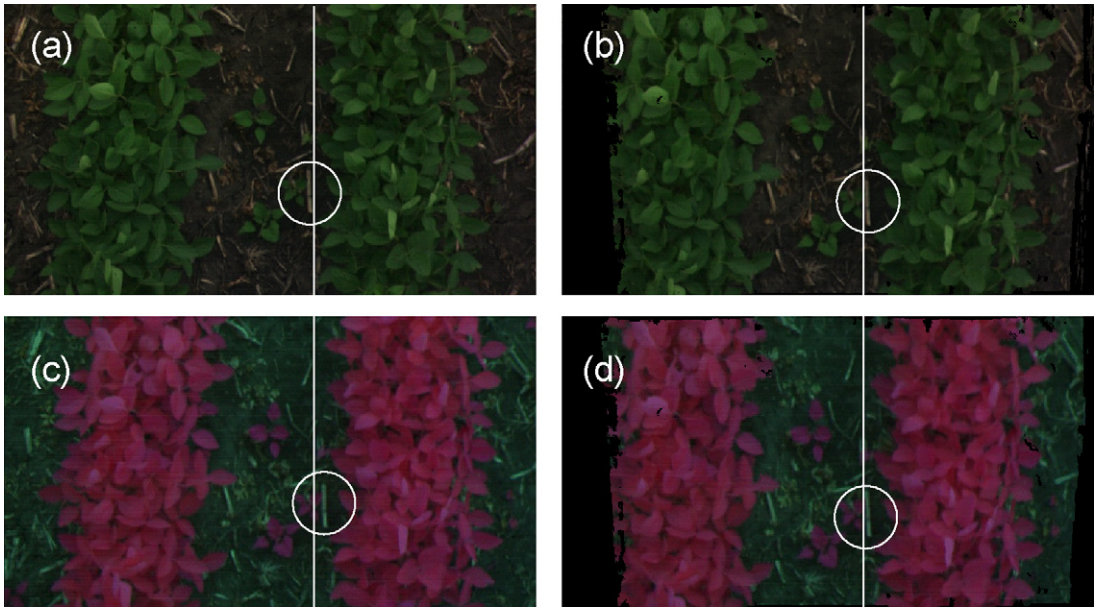

Fig. 4 – Example of stereovision-based image registration: (a) original left image; (b) processed left image; (c) original right image; and (d) processed right image. In the original image pair ((a) and (c)), a slight offset between the two images can be seen as indicated by the white line and circle; a dead plant in the circle of figure (a) is located left side of the line while same dead plant is located right side of the line in the figure (c); however, the dead plant is perfectly aligned after image registration shown in image (b) and (d).

the left camera coordinates can be uniquely determined from their geometric relationship. Two original images can be registered by the stereo computation, as demonstrated in Fig. 4. In the original image pair ((a) and (c)), a slight offset between two images can be seen due to the lateral offset of the viewpoint between the two cameras as indicated by the white line and circle; a dead plant in the circle in figure (a) is located left side of the line while the same dead plant is located on the right side of the line in the figure (c). Fig. 4(b and d) show the left and right images after stereo processing in which the images are accurately registered relative to each other as can be seen from the dead plants in the two images appearing in accurate alignment.

2.4. *Stereo image projection model for image mosaicing*

Recovering the changes of image geometry associated with camera motion is essential for image mosaicing. If two images are taken from the same viewpoint (but from different angles), or if two images are taken from different viewpoints but the scene is planar, the geometric relationship of those two images can be described by a 2D linear projective transformation called planar homography (Szeliski, 1996). Assume a given point in image frame 1, $m_1 = (x_1, y_1, w_1)^T$, representing the same object image frame 2, $m_2 = (x_2, y_2, w_2)^T$. The points m_1 and m_2 are represented in homogeneous coordinates and their corresponding Cartesian coordinates can be represented by $(x/w, y/w)^T$ (Foley et al., 1990). The geometric relationship of those two points in planar homography can be described by the following well known equation (Faugeras, 1993):

$$\begin{pmatrix} x_1 \\ y_1 \\ w_1 \end{pmatrix} = \begin{pmatrix} h_0 & h_1 & h_2 \\ h_3 & h_4 & h_5 \\ h_6 & h_7 & 1 \end{pmatrix} \begin{pmatrix} x_2 \\ y_2 \\ w_2 \end{pmatrix} \quad (1)$$

One of the major challenges faced in this research was that two images were taken from different viewpoints at non-planar scenes due to the features of an agricultural field, which made image mosaicing much more difficult than the methods of Eq. (1) could accommodate. Such a feature was attributed to the fact that the target scene in an agricultural field contains voluminous 3D objects (such as crop rows) and that the camera moves continuously within the field with both translational and rotational motions. To solve this problem, an image mosaicing algorithm developed in this research used the depth information at every pixel of the image. Based on this approach, Eq. (1) could be expanded to a fourth-order projective transformation by introducing the depth z as a new parameter of the point:

$$\begin{pmatrix} x_1 \\ y_1 \\ z_1 \\ w_1 \end{pmatrix} = \begin{pmatrix} h_0 & h_1 & h_2 & h_3 \\ h_4 & h_5 & h_6 & h_7 \\ h_8 & h_9 & h_{10} & h_{11} \\ h_{12} & h_{13} & h_{14} & 1 \end{pmatrix} \begin{pmatrix} x_2 \\ y_2 \\ z_2 \\ w_2 \end{pmatrix} \quad (2)$$

The equation can be represented in a matrix form as follows:

$$m_1 = Hm_2 \quad (3)$$

where, H is a 3D projection matrix which performs a crucial role in the image mosaicing algorithm.

With an assumption of the existence of some corresponding points in the two images, the simplest approach to compute 3D projection matrix is to find a matrix H_k that minimizes the following error function.

$$p_k = \sum_{i=0}^{n} \alpha_i \{(X_i^{(k-1)} - H_k X_i^{(k)})^T (X_i^{(k-1)} - H_k X_i^{(k)})\} \quad (4)$$

where, p_k is the error function to be minimized, $X_i^{(k-1)} = (x_i^{(k-1)}, y_i^{(k-1)}, z_i^{(k-1)}, w_i^{(k-1)})^T$ and $X_i^{(k)} = (x_i^{(k)}, y_i^{(k)}, z_i^{(k)}, w_i^{(k)})^T$ are the ith corresponding points in the two images taken at time instant $k-1$ and k, n the number of the corresponding points being found within two images, and α_i is the weight representing the degree of the correspondence.

It should be noticed that the 3D projection matrix H in Eq. (3) consists of both rotational and translational components. However, because the camera (and the platform vehicle) moves parallel to the ground, the components in the matrix H associated with the camera rotational motion are normally very small. To separate the rotational and translational motions of the camera, a 3D projection matrix H_k was rewritten as follows:

$$H_k = T_k D_k \quad (5)$$

where,

$$D_k = \begin{bmatrix} 1 & 0 & 0 & \delta_x \\ 0 & 1 & 0 & \delta_y \\ 0 & 0 & 1 & 0 \\ 0 & 0 & 0 & 1 \end{bmatrix}$$

is the translational matrix in which δ_x and δ_y represent lateral and longitudinal motions of the camera, respectively. To provide the location information of the images in the field, an RTK-GPS receiver, with its antenna mounted over the camera, was used to detect the translational motion of the camera between two images. A matrix T_k carries the rest of the information of H_k, namely the components related to the camera rotational motion and translational GPS measurement error, and is represented as follows:

$$T_k = I_4 + N_k \quad (6)$$

where, I_4 is a 4×4 unit matrix and N_k is a 4×4 error matrix representing camera rotation and GPS measurement errors.

As described above, camera rotational angles are normally small when being installed on a ground vehicle traveling within a field. By integrating Eq. (6) into Eq. (4), the error function can be reformed as follows:

$$p_k = \sum_{i=0}^{n} \alpha_i [(X_i^{(k-1)} - T_k D_k X_i^{(k)})^T (X_i^{(k-1)} - T_k D_k X_i^{(k)}) + \{(T_k - I)R\}^T \{(T_k - I)R\}] \quad (7)$$

where, R is a fourth-order gain vector and can be determined empirically. It should be noted that the second term on the right side represents the error matrix defined in Eq. (6).

Mathematically, T_k can be determined by minimizing p_k via partially differentiating Eq. (7) as follows:

$$T_k = \sum_{i=0}^{n} \alpha_i \{X_i^{(k-1)} (X_i^{(k)})^T D_k{}^T + RR^T\} \times \left[\sum_{i=0}^{n} \alpha_i \{D_k X_i^{(k)} (X_i^{(k)})^T D_k{}^T + RR^T\} \right]^{-1} \quad (8)$$

After all the above processes, the image projection from $X_i^{(k)}$ onto the panoramic image $Y_i^{(k)}$ can be represented in recursive form as follows:

$$\begin{cases} Y_i^{(k)} = G_k X_i^{(k)} \\ G_k = G_{k-1} T_k D_k \\ G_0 = I_4 \end{cases} \quad (9)$$

where, $Y_i^{(k)}$ is the image of $X_i^{(k)}$ projected onto the panoramic image coordinates. Eq. (9) indicates that stereo images are progressively projected onto the panoramic image coordinates.

2.5. *Feature point tracking*

To calculate a 3D projection matrix discussed in the previous section, it is necessary to identify corresponding points in two consecutive images. Theoretically, an ideal mosaic would be achieved if all corresponding points were found over the two images. However, considering the high computational load for searching all corresponding pixels over two images and the high risk of a large number being an incorrect match, it is more practical to select some distinctive feature points in one image and then search the corresponding points in another image. A feature point detector proposed by Harris and Stephens (1988) was used in this algorithm to detect the feature points. This detector uses a local auto-correlation function as the detecting operator (also known as Harris operator) to detect points with a distinctive feature. A large Harris operator (represented by η hereafter) suggests that there exists a large intensity variation in the neighboring area. Naturally, feature points can often be found at either the edge or the corner of an object. The target scenes of this research were agricultural fields with crop canopies, weeds, dead plants, crop residues and soil surfaces coexisting in an image frame. Such a multi-object coexistence resulted in a wide variation of the reflected radiations in different spectral bands. For example, the NIR and G bands often produced a larger η value for crop canopy pixels than that for the R and B bands while a soil surface with dead plants caused a larger η value in the R band than in other bands. To distribute feature points from crop canopy to soil background, a band-specific η determination approach that calculated η on all bands, and selected the largest η as the feature point detection was developed. In addition, to securely distribute the detected feature points over the image as uniformly as possible, the approach developed for feature point detection divided an image frame into 198 square windows of 30×30 pixels (as shown in Fig. 5), and the point with the largest η in a partic-

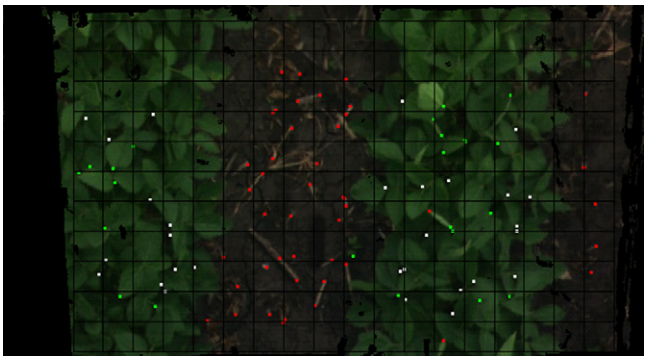

Fig. 5 – Example of feature point tracking. Red, green and white dots indicate the corresponding points found in the red (channel 3 of left camera), green (channel 2 of left camera) and NIR (channel 3 of right camera) bands, respectively. (For interpretation of the references to color in this figure legend, the reader is referred to the web version of the article.)

ular window was chosen as the feature point in the window. Supported by those two treatments, this approach could reliably detect the feature points represented by different kinds of objects with a fairly even distribution.

After feature points in a current image frame were selected, it was also necessary to search for the corresponding points in the preceding frame. The sum of the squared difference (SSD) algorithm was used as the indicator to determine the correspondence of two points (Scharstein, 1999).

Fig. 5 shows an example of the feature point tracking in a 3D soybean field image taken by the left camera. In this figure, the red, green and white dots indicate the corresponding points found in the red (channel 3 of left camera), green (channel 2 of left camera) and NIR (channel 3 of right camera) bands, respectively. A total of 99 points were tracked and successfully distributed over the sample image, with the points in the R band being mostly located in the soil region and the ones in G and NIR bands occurring in the canopy area.

3. Results and discussion

3.1. *Field image collection*

A series of field tests were conducted at the Agricultural Engineering Research Farm of the University of Illinois at Urbana-Champaign. From this series of field tests, streams of stereo images were collected while the research platform traveled over two soybean plots on the testing field. The same variety of soybeans was planted in both plots, but the soybeans in Plot 1 were planted 2 weeks after those planted in Plot 2. Consequently, this difference in planting time resulted in a noticeable size difference in the crops from the two plots. On the day the field images were collected, the majority of the crops were approximately 0.2 m and 0.5 m high on Plot 1 and Plot 2, respectively. The resolution of collected individual stereo images was 640×350 pixels which covered two crop rows 0.75 m apart. An image collection rate of 5 frames/s and the platform traveling speed of 0.5 m/s resulted in an overlapping zone of approximately 200 pixels in two consecutive images.

3.2. *Panoramic field image mosaics*

Fig. 6 shows a panoramic image assembled from 12 individual multi-spectral images taken on Plot 1. This is a composite image of channels 1 (CWL 478 nm) and 2 (537 nm) of the left camera, and channel 3 (796 nm) of the right camera. The research platform traveled upward in the image. The stereo images are progressively projected onto the panoramic image from the bottom of the image toward the top. The mosaic process was performed off-line using the image streams collected from field tests. It took about 20 s to complete a cycle of the mosaicing process from the stereo computation to image projection on a Windows-based PC (Pentium 4, 2.6 GHz with 2.0 GB RAM) with in-house developed software programmed in Microsoft Visual C++. This 640×1460 pixels portion of panoramic image represented a rectangle area of approximately 1.5 m $\times$ 3.4 m in the field.

From the Fig. 6, it is evident that the panoramic view of the soybean field was very well reconstructed as the seams of the constituent images are hardly noticeable over the resulting

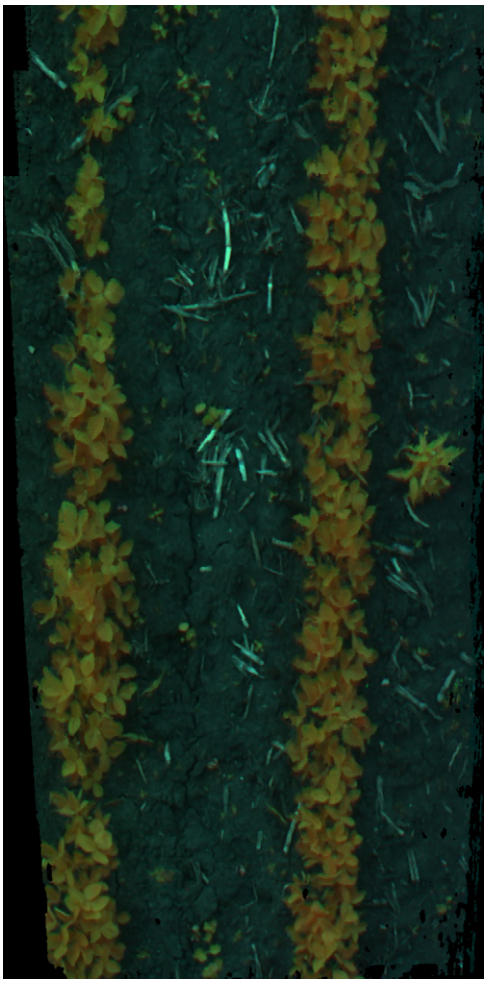

Fig. 6 – A panoramic multi-spectral field image (CWL 478, 537 and 796 nm) assembled from 12 constituent images taken at Plot 1 (with crop height of approximate 0.2 m).

Table 2 – Summary of image projection accuracy

	Image no.											
	0	1	2	3	4	5	6	7	8	9	10	11	Total
Overlapping pixels	0	112,000	142,000	140,000	137,000	132,000	159,000	120,000	160,000	113,000	101,000	125,000	1445,000
RMS of gray level errors	0	7.6	6.2	7.8	8.5	9.3	8.4	9.9	8.2	8.7	8.7	7.4	8.2

panoramic image. Because Fig. 6 is a three-band composite image, two of which are from the left camera and one from the right camera, the resulting panoramic image also proved that the images taken by two cameras could be accurately registered to create a six-spectral bands image.

To quantify the image projection accuracy, the gray level error of an overlapping pixel, defined as the gray level difference between pixels from different stereo images projected on the same location in the panoramic image, was computed as an indicator of the image projection error. The image recorded from channel 2 of the left camera was used for computing those errors. Table 2 summarizes the number of overlapping pixels and the root-mean square (RMS) of the calculated gray level errors. Since Image 0 was used as the base image to form the panoramic image, there is no overlapping region on this image. Any other images mapped to the panoramic image should have some overlap with the preceding image(s) for forming a seamless panoramic image. The number of overlapping pixels is roughly proportional to the length of the overlapping region in a longitudinal direction due to the moving direction of the camera. If some of the pixels in the mapping image were projected to a point where the pixels were already the projections of other images in previous mappings, then the gray level errors of those pixels should be calculated. An analysis of the calculated gray level error for Images 1–11 showed that the RMS error of the calculated gray levels was less than 10.0 for all 11 evaluated images. Such small RMS errors indicated a consistent accuracy of projection for the entire mosaicing process, and they further implied that the described image projection algorithm was capable of consistently forming a panoramic field view from the stream of stereo images.

Fig. 7 shows a histogram of gray level errors computed from all 12 images. Almost all the calculated gray level errors were distributed between −52 and 52. The calculated error outliers were less than 1.2% of the total calculated errors. By setting an error class with an error band of 5 and the minimal error class with an error range between −2.5 and 2.5, a total of 21 classes of error bands, with their center values of −50, −45, . . ., 0, . . ., 45, 50, respectively, were defined. The error histogram appeared as a normal distribution concentrated mostly at the center of the error distribution bands. Numerical analysis indicated that over 60% of the gray level errors fell in the range of ±5, 77% within ±10, and 90% within ±20.

Fig. 8 shows the mosaic image seamlessly assembled from 7 stereo images taken from Plot 2, where soybean plants were noticeably taller due to the earlier planting date. The assembled 640 × 800 pixel panoramic image represented an approximate 1.5 m × 1.9 m rectangle ROI in the field. The mosaic images shown here were a panoramic field view from the left camera (Fig. 8(a)) and an elevation map (Fig. 8(b)). A gray level in the elevation map indicates the height of an object at the corresponding location with a brighter pixel representing a higher elevation. The RMS error of the gray levels calculated from the constituent images was 9.8, indicating a high accuracy for the image projections.

One of the interesting applications for the panoramic field imaging system proposed in this research is the creation of a multi-spectral 3D virtual field scene. It is created by fusing the panoramic field image with the corresponding field elevation map. Fig. 9 shows examples of a 3D virtual field from different viewpoints, created by plotting the panoramic field image on the polygon surface of the field elevation map presented in Fig. 8 using Microsoft DirectX technology. This multi-spectral 3D virtual field scene could provide comprehensive crop growth information, including the crop size, density, weeds distribution and crop health information.

As a result of field testing, it was confirmed that the remote sensing system developed in this research could provide a field image fulfilling the three objectives stated in the introduction: (1) a field imagery created by a mosaic of the vehicle-mounted stereo camera image stream had a seamless panoramic view with high spatial resolution; (2) a six-spectral band image was obtained by the stereovision camera consisting of two multispectral cameras with different spectral configurations; (3) a 3D virtual field was created by fusing a 3D elevation map and panoramic field image.

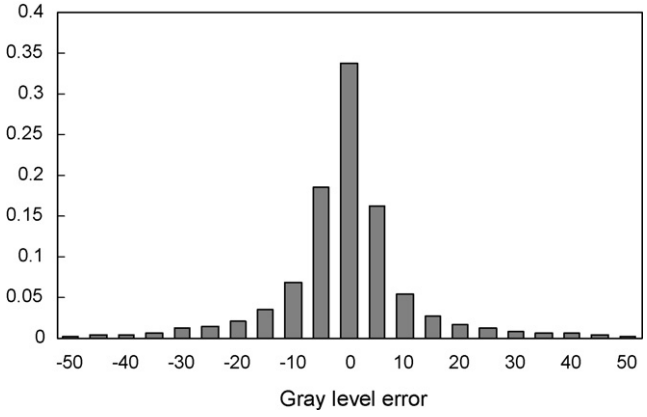

Fig. 7 – Histogram of gray level error for all 12 constituent images.

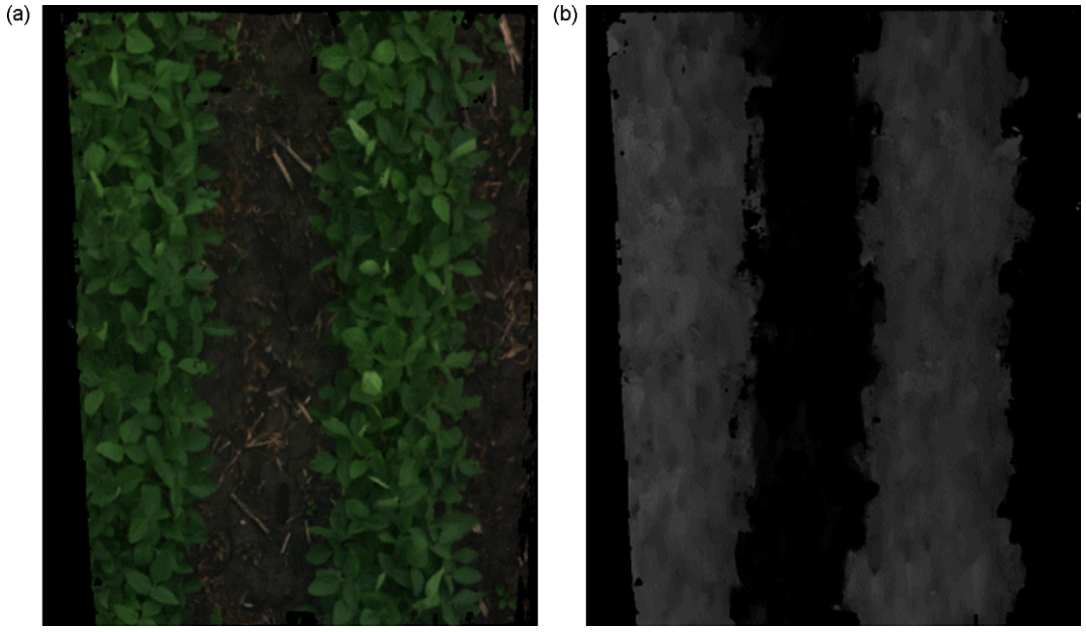

Fig. 8 – Panoramic multi-spectral field image (CWL 478, 537, and 621 nm) assembled from 7 images taken at plot 2 with an approximate crop height of 0.4 m in two forms: (a) the panoramic image from left camera and (b) the elevation map for the portion of the field.

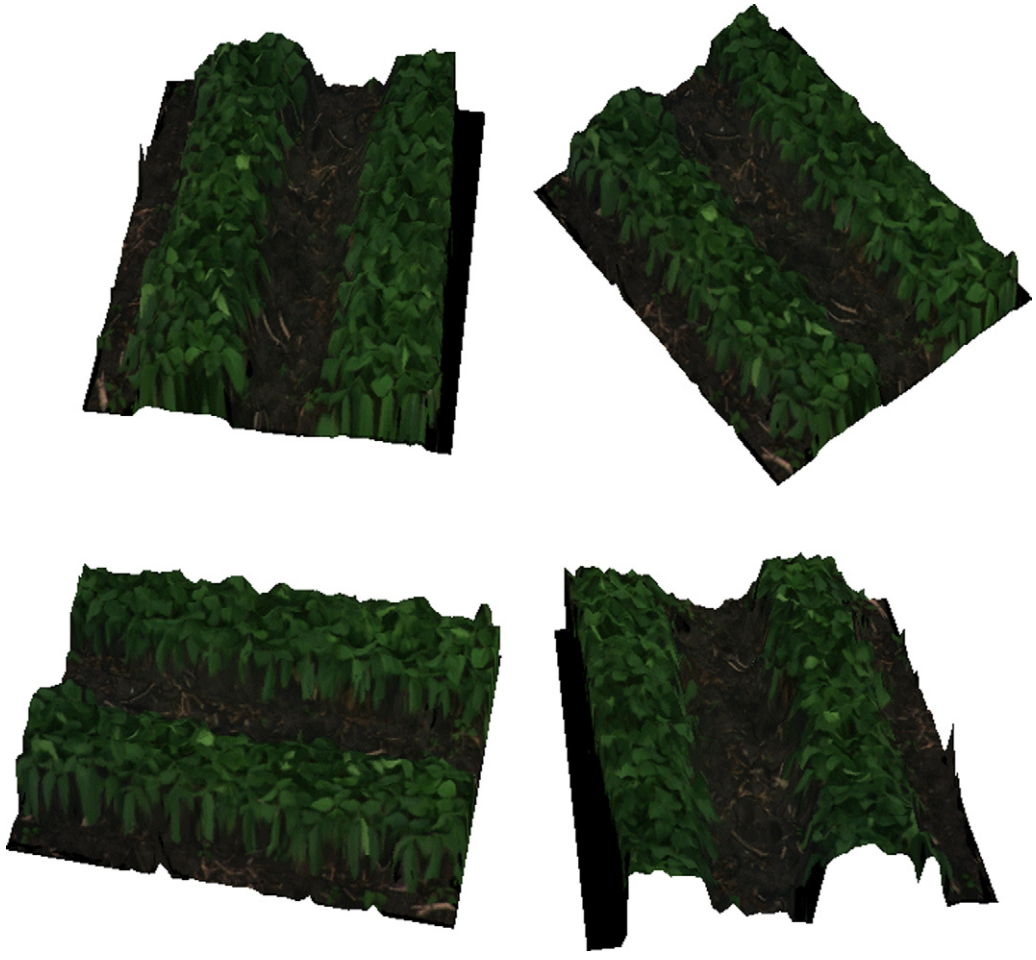

Fig. 9 – Examples of 3D virtual field images with various viewpoints created from the mosaic image and elevation map.

4. Conclusions

A ground-based remote sensing system that can provide a field image with a seamless panoramic view at high spatial resolution, three-dimensional (3D) information of plants, and multi-spectral reflectance was developed in this research. The sensor for the field sensing system was a stereovision camera composed of two multi-spectral cameras mounted on a ground vehicle. A stream of multi-spectral stereo field images was subsequently synthesized into one seamless image. Field test results verified that the 3D panoramic view of a soybean field could be reconstructed from a stream of stereo images. The panoramic field image, which contained six-spectral bands, provided a seamless view of the field. A virtual 3D field was also created from the panoramic field image together with a 3D elevation map. The new ground-based remote sensing method developed in this research offered more comprehensive, informative, and thorough data from an entire field in terms of spectral and biophysical field sensing than conventional remote sensing systems. Again, it should be pointed out that traditional remote sensing systems have an advantage in terms of the size of field coverage; hence it would be very helpful if we could take corresponding advantages from both traditional method and this developed method in terms of the specific applications.

Acknowledgements

The material presented in this paper was based upon work supported partially by Illinois Council on Food and Agricultural Research (IDA CF 99 SI-36-1A), Cowgur Mid-Tech Mechatronics Memorial Funds and USDA Hatch Funds (ILLU-10-352 AE). Japan Society for the Promotion of Science (JSPS) provided a Fellowship Fund to support Dr. Michio Kise in conducting his postdoctoral research at the University of Illinois at Urbana-Champaign. A 3D virtual image viewer program developed by Dr. Ryo Sugiura at Hokkaido University, Japan, was used in this research to support the development of the reported panoramic image formation method. All mentioned support is gratefully acknowledged. Any opinions, findings, and conclusions expressed in this publication are those of the authors and do not necessarily reflect the views of the University of Illinois, JSPS, Mid-Tech, Illinois CFAR or USDA.

REFERENCES

Bajwa, S.G., Tian, L.F., 2001. Aerial CIR remote sensing for weed density mapping in a soybean field. Trans. ASAE 44 (6), 1965–1974.

Cashion, J., Lakshmi, V., Bosch, D., Jackson, T.J., 2004. Microwave remote sensing of soil moisture: evaluation of TRMM microwave imager (TMI) satellite for the little river watershed Tifton, Georgia. J. Hydrol. 307, 242–253.

Datt, B., 1999. Remote sensing of water content in Eucalyptus leaves. Aust. J. Bot. 47 (6), 909–923.

Faugeras, O., 1993. Three-Dimensional Computer Vision. MIT Press, Cambridge.

Foley, J.D., Van Dam, A., Feiner, S.K., Hughes, J.F., 1990. Computer Graphics: Principles and Practice. Addison-Wesley, Reading.

Goel, P.K., Landy, J.A., Patel, R.M., Viau, A.A., Miller, J.R., 2003. Estimation of crop biophysical parameters through airborne and field hyperspectral remote sensing. Trans. ASAE 46 (4), 1235–1246.

Han, S., Hendrickson, L., Ni, B., 2002. Comparison of satellite and aerial imagery for detecting leaf chlorophyll content in corn. Trans. ASAE 45 (4), 1229–1236.

Harris, C., Stephens, M., 1988. A combined corner and edge detector. In: Proceedings of Fourth Alvey Vision Conference, Manchester, pp. 147–151.

He, D.X., Matsuura, Y., Kozai, T., Ting, K.C., 2003. A binocular stereovision system for transplant growth variables analysis. Appl. Eng. Agric. 19 (5), 611–617.

Kise, M., Zhang, Q., Rovira Más, F., 2005. A Stereovision-based crop row detection method for tractor-automated guidance. Biosyst. Eng. 90 (4), 357–367.

Lines, J.A., Tillett, R.D., Ross, L.G., Chan, D., Hockaday, S., McFarlane, N.J.B., 2001. An automatic image-based system for estimating the mass of free-swimming fish. Comput. Electron. Agric. 31 (2), 151–168.

Maxwell, S.K., Nucklos, J.R., Ward, M.H., Hoffer, R.M., 2004. An automated approach to mapping corn from Landsat imagery. Comput. Electron. Agric. 43 (1), 43–54.

Payero, J.O., Neale, C.M.U., Wright, J.L., 2004. Comparison of eleven vegetation indices for estimating plant height of alfalfa and grass. Appl. Eng. Agric. 20 (3), 385–393.

Rovira-Más, F., Zhang, Q., Reid, J.F., 2005. Creation of three-dimensional crop maps based on aerial stereo images. Biosyst. Eng. 90 (3), 251–259.

Scharstein, D., 1999. View Synthesis Using Stereo Vision. Lecture Note in Computer Science. Springer-Verlag, Berlin.

Shrestha, D.S., Steward, B.L., 2003. Automatic corn population measurement using machine vision. Trans. ASAE 46 (2), 559–565.

Szeliski, R., 1996. Video mosaics for virtual environments. IEEE Comput. Graph. Appl. 16 (2), 22–30.

Thomasson, J.A., Sui, R., Cox, M.S., Al-Rajehy, A., 2001. Soil reflectance sensing for determining soil properties in precision agriculture. Trans. ASAE 44 (6), 1445–1453.

Thomson, S.J., Zimba, P.V., Bryson, C.T., Alacorn-Calderon, V.J., 2005. Potential for remote sensing from agricultural aircraft using digital video. Appl. Eng. Agric. 21 (3), 531–537.

Tillett, N.D., Haugue, T., Miles, S.J., 2001. A field assessment of a potential method for weed and crop mapping on the basis of crop planting geometry. Comput. Electron. Agric. 32 (3), 229–246.

Van Niel, T.G., McVicar, T.R., 2004. Determining temporal windows for crop discrimination with remote sensing: a case study in South-Eastern Australia. Comput. Electron. Agric. 45 (1–3), 91–108.

Wright, G.G., Matthews, K.B., Tapping, J.C., 2003. Combining aerial photography and near-infrared videography to define within-field soil sampling frameworks. Geocarto Int. 18 (4), 1–8.

Wu, J., Tillett, R., McFarlane, N., Ju, X., Siebert, J.P., Schofield, P., 2004. Extracting the three-dimensional shape of live pigs using stereo photogrammetry. Comput. Electron. Agric. 44 (3), 203–222.

Yang, C., Bradford, J.M., Wiegand, C.L., 2001. Airborne multispectral imagery for mapping variable growing conditions and yields of cotton, grain sorghum, and corn. Trans. ASAE 44 (6), 1983–1994.